Bioactive Materials 18 (2022) 116–127

Contents lists available at ScienceDirect

Bioactive Materials

journal homepage: www.keaipublishing.com/en/journals/bioactive-materials

Orchestration of energy metabolism and osteogenesis by Mg^{2+} facilitates low-dose BMP-2-driven regeneration

Sihan Lin [a,b,c,d,e,f,1], Shi Yin [a,b,c,d,e,f,1], Junfeng Shi [a,b,c,d,e,f], Guangzheng Yang [a,b,c,d,e,f], Xutao Wen [g], Wenjie Zhang [a,b,c,d,e,f], Mingliang Zhou [a,b,c,d,e,f,**], Xinquan Jiang [a,b,c,d,e,f,*]

[a] Department of Prosthodontics, Shanghai Ninth People's Hospital, Shanghai JiaoTong University School of Medicine, No. 639 Zhizaoju Road, Shanghai, 200011, People's Republic of China
[b] College of Stomatology, Shanghai JiaoTong University, No. 639 Zhizaoju Road, Shanghai, 200011, People's Republic of China
[c] National Center for Stomatology, No. 639 Zhizaoju Road, Shanghai, 200011, People's Republic of China
[d] National Clinical Research Center for Oral Diseases, No. 639 Zhizaoju Road, Shanghai, 200011, People's Republic of China
[e] Shanghai Key Laboratory of Stomatology, No. 639 Zhizaoju Road, Shanghai, 200011, People's Republic of China
[f] Shanghai Engineering Research Center of Advanced Dental Technology and Materials, No. 639 Zhizaoju Road, Shanghai, 200011, People's Republic of China
[g] Department of Oral and Maxillofacial Surgery, College and Hospital of Stomatology, Guangxi Medical University, No. 10 Shuangyong Road, Qingxiu District, Nanning, Guangxi, 530021, People's Republic of China

ARTICLE INFO

Keywords:
Biomaterials
Bone morphogenetic protein-2
Magnesium
Energy metabolism
Bone regeneration

ABSTRACT

The clinical application of bone morphogenetic protein-2 (BMP-2) is limited by several factors, including ineffectiveness at low doses and severe adverse effects at high doses. To address these efficacy and safety limitations, we explored whether orchestration of energy metabolism and osteogenesis by magnesium ion (Mg^{2+}) could reduce the dose and thereby improve the safety of BMP-2. Our results demonstrated that rapid metabolic activation triggered by BMP-2 was indispensable for subsequent osteogenesis. Moreover, inadequate metabolic stimulation was shown to be responsible for the ineffectiveness of low-dose BMP-2. Next, we identified that Mg^{2+}, as an ''energy propellant", substantially increased cellular bioenergetic levels to support the osteogenesis via the Akt-glycolysis-Mrs2-mitochondrial axis, and consequently enhanced the osteoinductivity of BMP-2. Based on the mechanistic discovery, microgel composite hydrogels were fabricated as low-dose BMP-2/Mg^{2+} codelivery system through microfluidic and 3D printing technologies. An in vivo study further confirmed that rapid and robust bone regeneration was induced by the codelivery system. Collectively, these results suggest that this bioenergetic-driven, cost-effective, low-dose BMP-2-based strategy has substantial potential for bone repair.

1. Introduction

To date, bone morphogenetic protein-2 (BMP-2)-based therapy is the most widely used method for bone repair and has shown potent therapeutic effects [1]. However, BMP-2-based therapy is still hampered by factors such as ineffectiveness at low doses and severe complications at high doses [2]. To address this problem, considerable strategies, such as gene therapy, codelivery of growth factors (GFs), and delivery system modifications have been developed to amplify the efficacy of low-dose BMP-2. Gene therapy includes the delivery of BMP-2 genes or siRNA of BMP-2 antagonists to targeted sites, leading to the appropriate expression level of BMP-2 for the necessary duration [3,4]. Codelivery of BMP-2 with GFs, involves PDGF, SDF-1, VEGF enhances the BMP-2 efficacy via augmentation of stem cells recruitment and angiogenesis [5–7]. Modification of delivery system mainly focuses on improving the loading efficiency and sustained release of BMP-2 through the design of

Peer review under responsibility of KeAi Communications Co., Ltd.
* Corresponding author. Department of Prosthodontics, Shanghai Ninth People's Hospital, Shanghai JiaoTong University School of Medicine, No.639 Zhizaoju Road, Shanghai, 200011, People's Republic of China.
** Corresponding author. Department of Prosthodontics, Shanghai Ninth People's Hospital, Shanghai JiaoTong University School of Medicine, No.639 Zhizaoju Road, Shanghai, 200011, People's Republic of China.
E-mail addresses: zhoumingliang@aliyun.com (M. Zhou), xinquanjiang@aliyun.com (X. Jiang).
[1] These authors contributed equally.

https://doi.org/10.1016/j.bioactmat.2022.03.024
Received 3 January 2022; Received in revised form 26 February 2022; Accepted 13 March 2022
Available online 24 March 2022

biomaterials [8,9]. Nevertheless, translating these strategies from the bench to the bed side remains challenging due to their limitations, including safety and ethical concerns of gene editing [10], the use of GFs without regulatory approval [11], and complicated manufacturing procedures [9]. Therefore, a cost-effective and easy-to-follow low-dose BMP-2-based strategy is needed.

Bone formation is a highly metabolic process, as biosynthesis and biomineralization require large amounts of energy [12]. Emerging studies have indicated that metabolism is no longer a bystander but rather a key regulator that steers the outcome of bone regeneration [13–15]. BMP-2 plays a critical role in regulating bone formation, moreover, BMP signaling has been recently recognized to exert a regulatory role in energy metabolism in adipose tissue [16]. However, energy metabolism during osteogenesis remains an unexplored target of BMP-2, and whether it could influence BMP-2-driven bone regeneration is far from clear. It is worth noting that energy metabolism disturbances, such as diabetes mellitus, impair the outcome of BMP-2-induced bone formation, and metabolic mediators, such as insulin, potentiate the osteoinductivity of BMP-2 [17,18]. Therefore, we speculate that the ineffectiveness of low-dose BMP-2 is related to the inadequate activation of energy metabolism, and the incorporation of bioenergetic-active factors into biomaterials that enhance cellular metabolism to thereby meet the intense energy requirements for bone repair may be a new strategy to improve BMP-2 efficacy.

A recent study identified that the magnesium (Mg) concentration in mitochondria was vital to embryonic bone biomineralization, indicating that Mg might act as a bridge between metabolism and osteogenesis [19]. Moreover, as a cofactor of adenosine triphosphate (ATP), Mg^{2+} regulates the main metabolic pathways, glycolysis and oxidative phosphorylation (OxPhos), to profoundly affect cellular function [20,21]. For instance, by improving mitochondrial function, dietary supplementation with Mg could promote cardiac diastolic function in subjects with diabetes mellitus [22]. Inspired by this, we believe that a Mg-enriched microenvironment would increase the efficacy of low-dose BMP-2 via the orchestration of energy metabolism and osteogenesis.

Optimal platforms are pivotal for transferring the Mg^{2+}-based bioenergetic-driven BMP-2 delivery system into applications for high-performance bone regeneration. Hydrogel microgels, such as alginate microgels, are desirable vehicles owing to their unique properties, including good injectability, similarity to the native extracellular matrix, and considerable drug loading efficiency [23]. Moreover, affinity to divalent cations makes alginate an ideal carrier for Mg^{2+} [24], but some drawbacks remain. Typically, microgels display a fast release profile of encapsulated cargoes due to their porous structure and short diffusion distance. Moreover, consistently retaining microgels in defect areas is difficult due to their mobility, which may cause off-target side effects [23]. To solve these problems, we embedded microgels into methacrylated gelatin (GelMA) to construct a microgel composite hydrogel. GelMA held the microgels at defects and acted as a secondary diffusion barrier to reduce the adverse effects of fast release, and the microgels, in return, reinforced the physiological and mechanical properties of the whole system.

Here, to address the safety and efficacy issues regarding BMP-2-based therapy, a Mg^{2+}-based bioenergetic-driven strategy was developed to improve low-dose BMP-2-driven regeneration by orchestrating energy metabolism and osteogenesis. A series of experiments indicated that successive activation of glycolysis and OxPhos triggered by BMP-2 was the prerequisite for subsequent osteogenesis, and inadequate energy status resulted in the ineffectiveness of low-dose BMP-2. Mg^{2+}, as an "energy propellant", increased the mitochondrial membrane potential ($\Delta\Psi m$) and upregulated the expression levels and activities of metabolic enzymes via the Akt signaling pathway. Elevated glycolysis and OxPhos by Mg^{2+} increased cellular bioenergetic levels to fuel osteogenesis, and thereby markedly promoted the osteoinductivity of BMP-2. Furthermore, the Mg^{2+} intake through Mg^{2+} channel mitochondrial RNA splicing 2 (Mrs2) facilitated the promotional effects of Mg^{2+}. Based on these findings, microgel composite hydrogels with Mg^{2+} as an energy propellant were fabricated as a low-dose BMP-2 delivery platform through microfluidic and 3D printing technologies (Schematic 1). Finally, high-performance bone regeneration induced by the delivery platform was observed in an animal model. Taken together, our Mg^{2+}-based bioenergetic-driven strategy provides new approaches for effective BMP-2-based therapy.

2. Experimental section

Animals: C57BL/6 mice and Sprague–Dawley (SD) rats were provided by Ninth People's Hospital Animal Center (Shanghai, China). All the experimental procedures utilized in the present study were approved by the Animal Care and Experiment Committee of the Ninth People's Hospital.

BMSC isolation and culture: Rat bone marrow stem cells (BMSCs) were isolated from 3-week-old SD rats and cultured as previously described [25]. Briefly, cells were washed from femurs and tibias and cultured in complete growth medium comprising low-glucose Dulbecco's modified Eagle medium (DMEM) (HyClone, USA), 10% fetal bovine serum (Gibco, USA), and 1% streptomycin and penicillin (HyClone, USA) at 37 °C in a 5% CO_2 atmosphere. Cells at passages 2–4 were used for the subsequent experiments.

In vitro optimization of the synergistic concentrations of BMP-2 and Mg^{2+}: To verify the optimal Mg^{2+} concentration, BMSCs were cultured in DMEM with Mg^{2+} at gradient concentrations (1.6×10^{-3}, 2.5×10^{-3}, 5×10^{-3}, 10×10^{-3}, 20×10^{-3} mol L^{-1}) and 100 ng mL^{-1} rh-BMP-2 (Rebone, China). DMEM with 0.8×10^{-3} mol L^{-1} Mg^{2+} was used as a control. For each group in each experiment, 3 replicates were performed. After incubation for a week, alkaline phosphatase (Alp) staining was conducted with an Alp staining kit (Beyotime, China) in accordance with the manufacturer's instructions. For quantitative analysis of Alp activity, Alp semiquantitative assays were performed via an Alp semiquantitative kit (Beyotime, China) according to the supplier's instructions, and the Alp activity was calculated based on the optical density (OD) at 405 nm per milligram of total protein. Total RNA was extracted using RNAiso Plus (TaKaRa, Japan) and then reverse-transcribed into complementary DNA (cDNA) for subsequent qPCR assays. The expression of osteogenesis-related genes was analyzed via the $2^{-\Delta\Delta CT}$ method. The primer sequences used in the experiments are provided in Table S1 (Supporting information). To evaluate the promotional effects of Mg^{2+} on low-dose BMP-2, we fixed the Mg^{2+} concentration at 5×10^{-3} mol L^{-1}, and the BMP-2 concentration decreased from 100 to 20 ng mL^{-1}. Alp staining and Alp semiquantitative analyses were carried out after one week of incubation. For mineralization analysis, Alizarin red S staining (ARS) was performed with 0.1% Alizarin red S (Sigma, USA) at 14 days after treatment. For quantitative analysis, Alizarin red S was dissolved in 10% cetylpyridinium chloride (Sigma, USA) for 60 min at room temperature. The calcium concentrations were determined by the OD value at 562 nm. The quantitative result was expressed as absorbance OD_{562} values per milligram of total protein. Moreover, the expression level of the osteogenesis marker osteocalcin (Ocn) was detected 7 days after induction with Mg^{2+} and different concentrations of BMP-2 via immunofluorescence staining. BMSCs were fixed and incubated with a primary antibody targeting Ocn (1:200 dilution, Proteintech, 23418-1-AP, USA) at 4 °C overnight. An Alexa Fluor 594-conjugated donkey anti-rabbit secondary antibody (1:200 dilution, Yeasen, 34212ES60, China) was used before the cell cytoskeleton and nuclei were stained with FITC-phalloidin (Yeasen, China) and 4′,6-diamidino-2-phenylindole (DAPI; Solarbio, China).

Subcutaneous implantation of BMP-2/Mg^{2+} microbeads and relevant radiological/histological evaluations: BMP-2 solution at different concentrations was dissolved in 6% (w/v) sodium alginate (SA) solution with 5×10^{-3} mol L^{-1} Mg^{2+}. The final concentrations of BMP-2 were 0, 20, 50, and 100 μg mL^{-1}. The microbeads were fabricated by dropping the mixture into 0.1 mol L^{-1} $CaCl_2$ and then injected subcutaneously

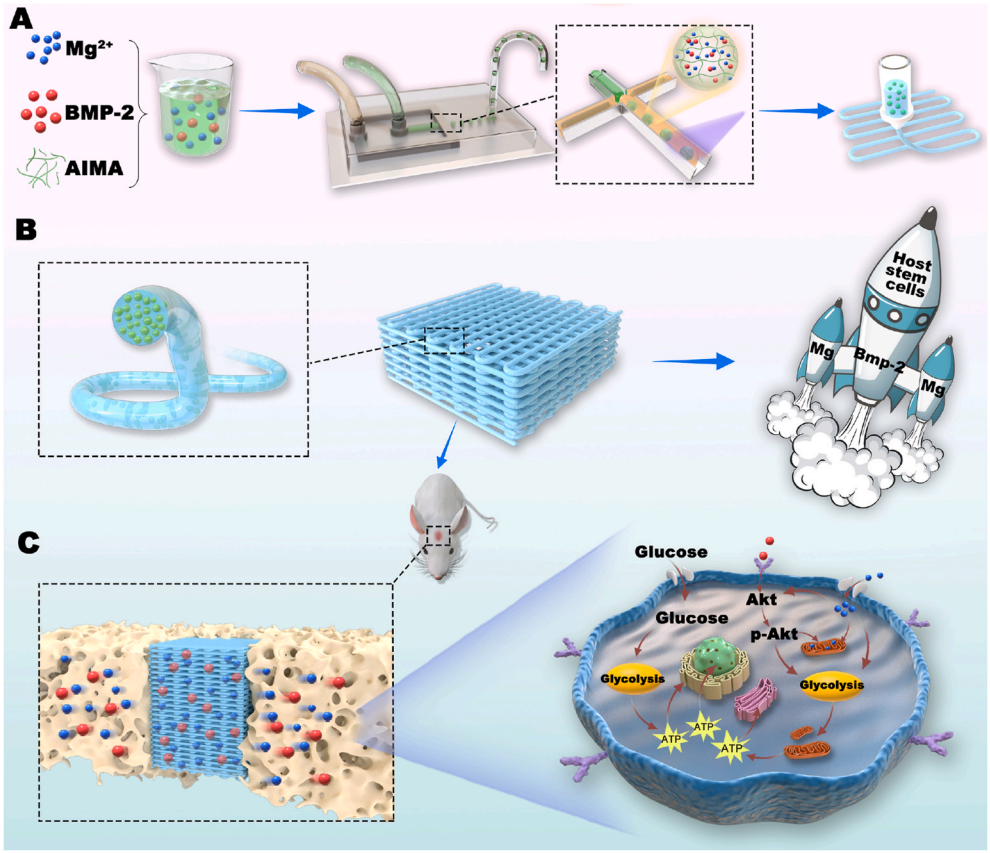

Schematic 1. By orchestrating energy metabolism and osteogenesis, the bioenergetic-driven microgel composite hydrogel with Mg^{2+} as an energy propellant constructed herein was shown to improve low-dose BMP-2-driven bone regeneration. A) Using microfluidic devices and a water-in-oil strategy, methacrylated alginate (AlMA) microgels containing Mg^{2+} and BMP-2 were fabricated. The microgels were then embedded in GelMA for the subsequent 3D printing of a microgel composite hydrogel scaffold. B) "Propelled" by BMP-2 and Mg^{2+}, the hydrogel functioned as a "cell shuttle" to drive the osteogenic differentiation of host stem cells. C) Mg^{2+}, as the "energy propellant" of the "shuttle", significantly improved the osteoinductivity of BMP-2 by activating the main metabolic pathways to thereby fuel the bioenergetic demand related to osteogenesis.

into mice (3 replicates in each group). Seven and fourteen days after implantation, the mice were sacrificed for angiogenesis and osteogenesis evaluation, respectively. Radiological imaging and quantitative analysis of bone formation were performed using a micro-CT system (μCT50, Scanco Medical, Switzerland). For histological analysis, samples were decalcified with a 20% EDTA solution, embedded in paraffin and sliced. H&E and Masson trichrome staining (Leagene, China) were conducted according to the manufacturers' protocols. Furthermore, the sections were incubated with Alp (1:50 dilution, R&D Systems, AF2910, USA), phosphofructokinase 1 (Pfk1) (1:100 dilution, Novus, NBP2-75578, USA), isocitrate dehydrogenase 2 (Idh2) (1:100 dilution, Novus, NBP2-22166, USA), and CD31 (1:50 dilution, R&D Systems, AF3628, USA) primary antibodies, and images were captured by fluorescence microscopy (Olympus, Japan).

Assessing the relation between energy metabolism and BMP-2-based osteogenesis: The oxygen consumption rates (OCRs) and the extracellular acidification rates (ECARs) were monitored by a Seahorse XF24 analyzer (Agilent Technologies, USA). BMSCs induced by 100 ng mL^{-1} BMP-2 were analyzed as the designated time points. Briefly, cells were seeded in XF24 microplates (Agilent Technologies, USA) at 10^5 cells per well and stabilized overnight. For the OCRs test, oligomycin, carbonyl cyanide 4- (trifluoromethoxy) phenylhydrazone (FCCP) and rotenone/antimycin A (Rot/AA) were sequentially injected at final concentrations of 1×10^{-6} mol L^{-1}. Alternatively, a glycolysis test was performed via the sequential addition of glucose (10×10^{-3} mol L^{-1}), oligomycin (1×10^{-6} mol L^{-1}) and 2-DG (50×10^{-3} mol L^{-1}). Data were normalized to seeded cell number, and key parameters of mitochondrial oxygen consumption and glycolysis were calculated as previously described [26,27]. To further investigate the gene expression profile during stimulation, total RNA was extracted from BMSCs at the designated time point, and cDNA was synthesized for qPCR analysis. The primer sequences used are provided in Table S1. Moreover, 2-deoxyglucose (2-DG) (50×10^{-3} mol L^{-1}) and LW6 (30×10^{-6} mol L^{-1}) were added to the medium to inhibit glycolysis and the TCA cycle, respectively. Seven days later, total protein was collected for Western blot analysis. A specific primary antibody against Ocn (1:200 dilution, Santa Cruz, sc-390877, USA) was used to evaluate osteogenic differentiation, actin (1:1000 dilution, CST, 3700S, USA) was used for normalization, and biomineralization was analyzed via ARS and quantitative assay. For signaling pathway investigation, Akt and p-Akt antibodies (1:1000 dilution, CST, 9272S, 9271T, USA) were used to confirm the phosphorylation of the Akt protein. Furthermore, the Akt inhibitor MK2206 (0.1×10^{-6} mol L^{-1}, MCE, USA) was applied to elucidate the influence of the Akt pathway on BMP-2-triggered metabolic alterations and osteogenesis. To evaluate energy production in BMSCs treated with MK2206, intracellular ATP levels were determined with an ATP assay kit (Solarbio, China) according to the manufacturer's instructions. Briefly, on day 7, the BMSCs culture medium was replaced with fresh complete growth medium 1 h before detection. The cell lysate was added to plates and mixed with a working solution. The relative intracellular ATP level was determined based on the OD_{340} normalized to the mass of the samples. For osteogenic differentiation, Alp staining and quantitative assay of BMSCs with MK2206 were performed on day 7. To verify the dose-dependent effects of BMP-2 on metabolic reprogramming, media containing 0, 20, 50, and 100 ng mL^{-1} BMP-2 were utilized. Total protein was collected at 15, 30, and 60 min after exposure to BMP-2 for the detection of Akt phosphorylation. The protein expression levels of Pfk and Idh were evaluated by immunofluorescence staining with the antibodies mentioned above. A JC-1 kit (Solarbio, China) was used to measure the ΔΨm of BMSCs according to the supplier's instructions. JC-1 aggregated in mitochondria with a high ΔΨm and emitted red fluorescence, and green fluorescence indicated free JC-1 in mitochondria with a low ΔΨm. For each group in seahorse analysis, 8 replicates were performed; while 3 replicates for each group in other experiments.

Impacts of Mg^{2+} on BMP-2-induced metabolic alteration: Measurement of Mg^{2+} entry and mitochondrial Mg^{2+} intake was conducted

through confocal laser scanning microscopy (CLSM, Leica, Germany). BMSCs were incubated with the Mg^{2+} probe Mag-Fluo-4 AM (2.5×10^{-6} mol L^{-1}, green fluorescence, MKBio, China) and the mitochondrial indicator MitoTracker Red CMXRos (0.5×10^{-6} mol L^{-1}, Yeasen, China) in growth medium at 37 °C for 30 min. Then, the cells were washed twice with Ca^{2+} and Mg^{2+}-free HBSS, and the medium was refreshed. After 40 s of baseline recording, PBS or BMP-2 was added, and after 240 s, 10×10^{-3} mol L^{-1} Mg^{2+} was added. Moreover, the dynamic changes in Mg^{2+} fluorescence intensity in 10 random mitochondrial regions were calculated via CLSM software. The OCRs, ECARs, gene expression profile, activation of the Akt pathway, and intracellular ATP level in BMSCs were detected in accordance with the aforementioned protocols after 7 days of incubation with 20 ng mL^{-1} BMP-2 with or without 5×10^{-3} mol L^{-1} Mg^{2+}. For the quantitative analysis of ΔΨm, cells were stained with JC-1 solution at 37 °C for 20 min, and cell sorting was then carried out on a flow cytometer (MoFlo XDP, Beckman, USA). The relative ΔΨm was calculated by the ratio of the mean intensities of red and green fluorescence. The activities of metabolic enzymes were determined with Pfk, pyruvate dehydrogenase (Pdh), and Idh activity assay kits (Solarbio, China) after 7 days of stimulation, and data were normalized to the mass or total protein of samples in accordance with the suppliers' protocols. The targeted knockout of Mrs2 was carried out using the CRISPR/Cas9 system (Genomeditech, China), and mutations in the Mrs2 sequences were identified by gene sequencing (Genomeditech, China). To evaluate the effects of Mrs2 disruption on BMP-2/Mg-induced metabolic and osteogenic alterations, dynamic imaging of Mg^{2+} influx and mitochondrial Mg^{2+} uptake, ATP production, Alp staining and quantitative analysis were performed. For each group in seahorse analysis, 6 replicates were performed; while 3 replicates for each group in other experiments.

Fabrication and characterization of microgel composite hydrogels: Microgels were fabricated using a water-in-oil strategy via a microfluidic technique. Briefly, a 6% (w/v) AlMA (EFL, China) solution containing BMP-2 and Mg^{2+} was dispersed in corn oil (Sigma, USA) mixed with 1 wt % Span 80 (Sigma, USA). The flow rate of the oil phase (Q_o) was fixed at 10 mL h^{-1}, and the flow rate of the aqueous phase (Q_{aq}) was varied to optimize the diameter of the microspheres. The droplets were exposed to UV radiation at the outlet of the microfluidic device (MesoBioSystem, China) for gelation and then washed with distilled water and embedded in 6% (w/v) GelMA (EFL, China) for 3D printing (Bioscaffold3.1, GeSiM, Germany). Microgel morphology was assessed using a brightfield microscope (Olympus, Japan) and NIH ImageJ software (100 microgels per group). The swelling behavior and degradation of hydrogels with different AlMA microgel contents were detected as previously described [28,29]. The hydrogels were subjected to compression analysis after reaching swelling equilibrium via a universal testing machine (HY-0230, Hengyi, China) at a speed of 10 mm min^{-1}. The rheological properties of the hydrogels were assessed via a rotation rheometer (HAKKE MARS 60, Germany). For strain-sweep tests, at a temperature of 37 °C and a frequency of 1 Hz, the shear strain was gradually increased from 0.1% to 1000%. The tests were conducted three times. The release of BMP-2 and Mg^{2+} was measured with ELISA kits (R&D Systems, USA) and QuatiChrom magnesium assay kits (BioAssay Systems, USA). First, the microgel washing liquid was collected to calculate the loading efficiency as previously described [30]. Then, 500 μL of the microgels and composite hydrogel with the same concentrations of BMP-2 and Mg^{2+} was immersed in 500 μL of PBS supplemented with 1% streptomycin and penicillin at 37 °C. At the designated time points, the supernatant was collected for BMP-2 and Mg^{2+} measurement. To evaluate the distribution of microgels in the hydrogel, red fluorescence-conjugated AlMA (EFL-FL-Alg-R, EFL, China) was observed under a fluorescence microscope. The biocompatibility tests were performed 14 days after the BMSCs were seeded on the composite hydrogels. In brief, the hydrogels were washed with PBS and fixed with 4% paraformaldehyde for 30 min at room temperature. A primary antibody targeting osteopontin (Opn) (1:50 dilution, R&D Systems, AF808, USA) was used to evaluate osteogenic differentiation. For swelling and compression tests, 4 replicates were conducted in each group; for degradation test, 4 samples were involved in each group at designed time point, while 3 replicates were performed in other experiments.

In vivo assay of the regenerative efficacy of Mg^{2+}-based bioenergetic-driven BMP-2 delivery platforms: Six-week-old SD rats were used to construct a critical cranial defect model. Two full-thickness defects with a diameter of 5 mm were made on both sides of the rat skull, and hydrogels from the following five groups (5 replicates in each group) were implanted: GelMA-encapsulated AlMA microgels (Control), GelMA-encapsulated AlMA microgels with 20 μg mL^{-1} BMP-2 (0.8 μg), GelMA-encapsulated AlMA microgels with 20 μg mL^{-1} BMP-2 (0.8 μg) and 5×10^{-3} mol L^{-1} Mg^{2+} (4.8 μg), and GelMA-encapsulated AlMA microgels with 50 or 100 μg mL^{-1} BMP-2 (2 μg and 4 μg of BMP-2, respectively). Defects without hydrogels were taken as blank controls. Samples were harvested at 4 weeks after surgery and subjected to X-ray imaging (Faxitron, USA) and micro-CT analysis. The samples were then decalcified in a 20% EDTA solution and embedded in paraffin for subsequent histological examination. H&E, Masson trichrome and immunofluorescence staining were conducted according to the manufacturers' instructions. To further evaluate osteogenesis, 4 random images from each group were selected to calculate the positive areas of Opn and Sp7 (1:200 dilution, Abcam, ab209484, UK) via NIH ImageJ software.

Statistical analysis: All data are displayed as the mean ± standard deviation. Statistical analyses were performed using GraphPad Prism 8 statistical software (GraphPad, USA). The normality distribution of the data was confirmed through the Shapiro-Wilk test, while the outlier was identified by Grubbs' test. Significant differences were indicated by $p < 0.05$ or $p < 0.01$ as determined by Student's *t*-test or one-way analysis of variance (ANOVA) followed by Tukey's post-hoc test for multiple comparisons.

3. Results and discussion

3.1. Optimization of synergistic concentrations of BMP-2 and Mg^{2+} in vitro

As previous studies reported, a moderate Mg^{2+}-enriched environment exerted positive effects on osteogenesis, while a high concentration of Mg^{2+} (i.e., 16×10^{-3} mol L^{-1}) inhibited the activities of osteoblasts [31,32]; thus, the influence of Mg^{2+} on the osteogenesis of BMSCs was strongly dose-dependent. Hence, to determine whether Mg^{2+} exerts a regulatory effect on BMP-2-mediated osteogenesis, we cultured BMSCs in medium containing BMP-2 and different concentrations of Mg^{2+} ranging from 1.6 to 20×10^{-3} mol L^{-1}, and BMP-2 with a physiological Mg^{2+} concentration (0.8×10^{-3} mol L^{-1}) was used as the positive control. The activity of Alp and the expression levels of osteogenesis-related genes in each group were evaluated. As shown in Fig. 1A and Fig. S1, when the concentration of BMP-2 was fixed at 100 ng mL^{-1}, the activity of Alp gradually increased as the Mg^{2+} concentration increased, and Alp exhibited the highest activity at a Mg^{2+} concentration of 5×10^{-3} mol L^{-1}. Further increasing the Mg^{2+} concentration led to a decrease in the activity of Alp, and when the Mg^{2+} concentration exceeded 10×10^{-3} mol L^{-1}, the activity of Alp gradually decreased to the level of that in the positive control group. As expected, the changes in osteogenic gene expression showed a similar trend, exhibiting a reverse U-shaped curve with a peak at 5×10^{-3} mol L^{-1} Mg^{2+} (Fig. 1B i-iv). As a result, we selected 5×10^{-3} mol L^{-1} as the optimum Mg^{2+} concentration to improve the BMP-2-driven osteogenesis. Next, to determine whether Mg^{2+} could enhance the efficacy of low-dose BMP-2, BMSCs were induced by different doses of BMP-2 together with Mg^{2+} at a concentration of 5×10^{-3} mol L^{-1}. Alp staining and ARS were employed to detect BMSC mineralization. Fig. 1C displayed the significant dose-dependent effects of BMP-2 on osteogenic differentiation of BMSCs. As the BMP-2 concentration decreased, the

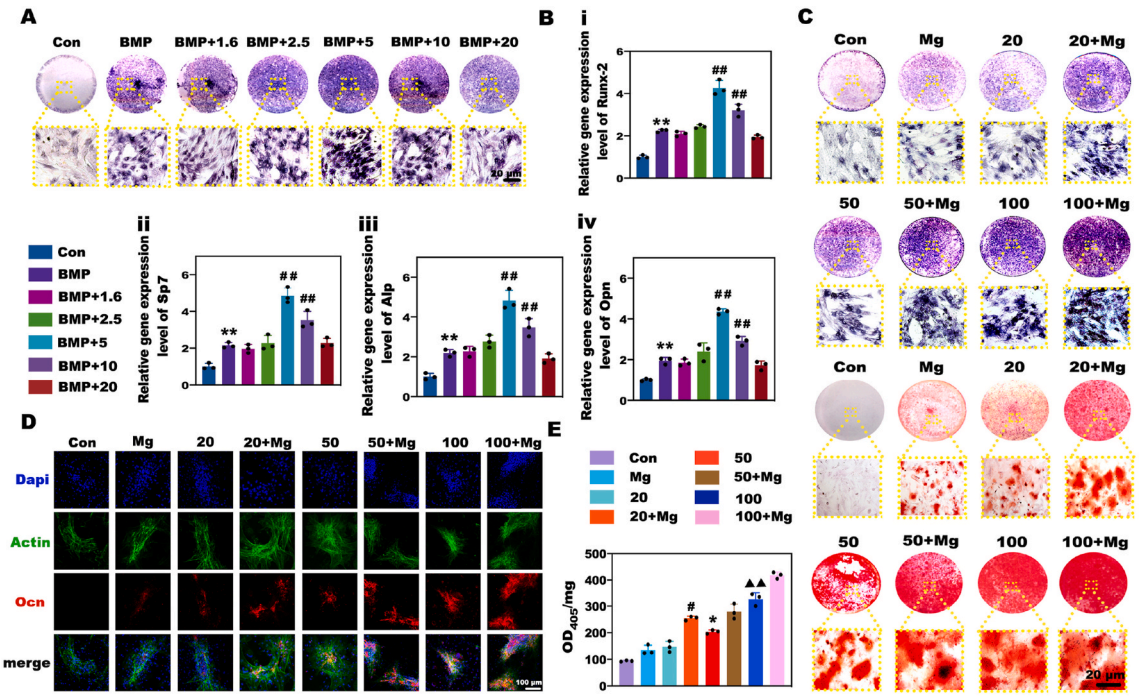

Fig. 1. In vitro evaluation of the effects of Mg^{2+} on BMP-2-mediated osteogenic differentiation. A) Alp staining of BMSCs treated with medium containing BMP-2 and gradient concentrations of Mg^{2+}. B) qPCR analysis of osteogenic gene expression in BMSCs. (** and ## represent $p < 0.01$ in comparison with the Con and BMP-2 groups, respectively). C) Alp staining and ARS of BMSCs induced by different doses of BMP-2 with or without an Mg-enriched environment. D) Immunofluorescence staining of the Ocn protein in BMSCs. E) Semiquantitative analysis of Alp activity in BMSCs to verify the promotional effects of Mg^{2+} on BMP-2-based osteogenesis. (# and * represent $p < 0.05$ in comparison with the 50 and 20 ng mL^{-1} groups, respectively; ▲▲ represents $p < 0.01$ in comparison with the 20 ng mL^{-1} + Mg group).

efficacy of BMP-2 declined drastically, and the mineralization level induced by 20 ng mL^{-1} BMP-2 was similar to that induced by Mg^{2+} alone. Nevertheless, the biomineralization in the groups induced by BMP-2 and Mg-enriched environments was markedly stronger than that in the groups treated with BMP-2 at the same concentration. Detection of the protein expression of Ocn, an osteogenic marker, further confirmed the upward tendency in the Mg-enriched groups (Fig. 1D). Notably, quantitative analysis of Alp activity and ARS revealed that Mg^{2+} increased the osteogenic bioactivity of 20 ng mL^{-1} BMP-2 to a higher level than that achieved with 50 ng mL^{-1} and close to that achieved with 100 ng mL^{-1} (Fig. 1E, Fig. S2). Based on the above results, Mg^{2+} showed great potential for improving the efficacy of BMP-2 for osteogenesis in vitro, and 5×10^{-3} mol L^{-1} was considered to be the optimum concentration for establishing the Mg-enriched environment.

3.2. *The promotional effect of Mg^{2+} on BMP-2 efficacy was related to an increase in metabolic activities*

Encouraged by the in vitro results, we further investigated the osteoinductivity of BMP-2/Mg^{2+} codelivery in vivo using a subcutaneous ectopic bone formation mouse model. SA is an ideal GFs delivery vehicle due to its easy gelation process and maintenance of GFs bioactivity [33]. Moreover, its affinity for divalent cations makes it an attractive carrier for Mg^{2+}. Hence, we fabricated SA microbeads encapsulating BMP-2 (final concentration varied from 20 μg mL^{-1} to 100 μg mL^{-1}) with or without Mg^{2+} (final concentration was 5×10^{-3} mol L^{-1}) for subcutaneous injection (Fig. 2A). The samples were collected at 2 weeks after surgery for radiological and histological analyses. Radiological imaging demonstrated that new bones were rarely observable in the groups without BMP-2, possibly owing to the lack of host stem cell recruitment initiated by BMP-2. Although decreases in the BMP-2 dose markedly compromised ossification, the Mg-enriched environment sharply promoted bone formation in the low-dose BMP-2 groups (Fig. 2B and C). Notably, in contrast to the 20 μg mL^{-1} group, robust bone formation was observed in the 20 μg mL^{-1} + Mg group, which was superior to that in the 50 μg mL^{-1} group and similar to that in the 100 μg mL^{-1} group. Moreover, though there was more bone formation in 50 μg mL^{-1} + Mg than 20 μg mL^{-1} + Mg groups, the difference between the two groups was not significant. It was worth noting that a dramatic increase of newly formed bone induced by Mg^{2+} addition was observed at 20 μg mL^{-1} BMP-2; when the doses increased, the promotional effects of Mg^{2+} on BMP-2 were not quite obvious. We deduced that Mg^{2+} exerted a different level of promotional effects on cells activated by different doses of BMP-2, leading to the no significant difference between 50 μg mL^{-1} + Mg and 20 μg mL^{-1} + Mg groups. Accordingly, histological analysis also revealed more new bones and a more active bone formation process around the microbeads in the BMP-2/Mg codelivery groups than in the other groups (Fig. 2D).

Interestingly, as indicated by the arrows in Fig. 2D, numerous blood vessels were formed in the new bone area, and vascularization was rather obvious in the Mg-enriched groups. Angiogenesis evaluation was further performed via immunofluorescent staining of CD31, a well-recognized marker for vascular endothelial cells [34], of samples collected a week after surgery (Fig. S3). Accordingly, the CD31 positive area increased as the BMP-2 doses increased, and there were more $CD31^{+}$ blood vessels in Mg-enriched groups than BMP-2 alone groups. It is well known that the bone vasculature plays a significant role in supplying the nutrients and oxygen needed for bone formation, and increased blood perfusion might represent an adaptive response to increased energy demand. To explore the metabolic status in the bone-forming area, we conducted colocalization analysis on Alp with markers of glycolysis and the tricarboxylic acid (TCA) cycle, including the rate-limiting enzymes Pfk and Idh. No obvious Pfk or Idh expression was detected in the limited Alp-positive region in the 20 μg mL^{-1} group, while the expression levels of metabolic enzymes in the abundant Alp-positive area increased as the BMP-2 dose increased, suggesting a strong relationship between bone formation and energy metabolism (Fig. 2E). Notably, a recent study reported that energy metabolism

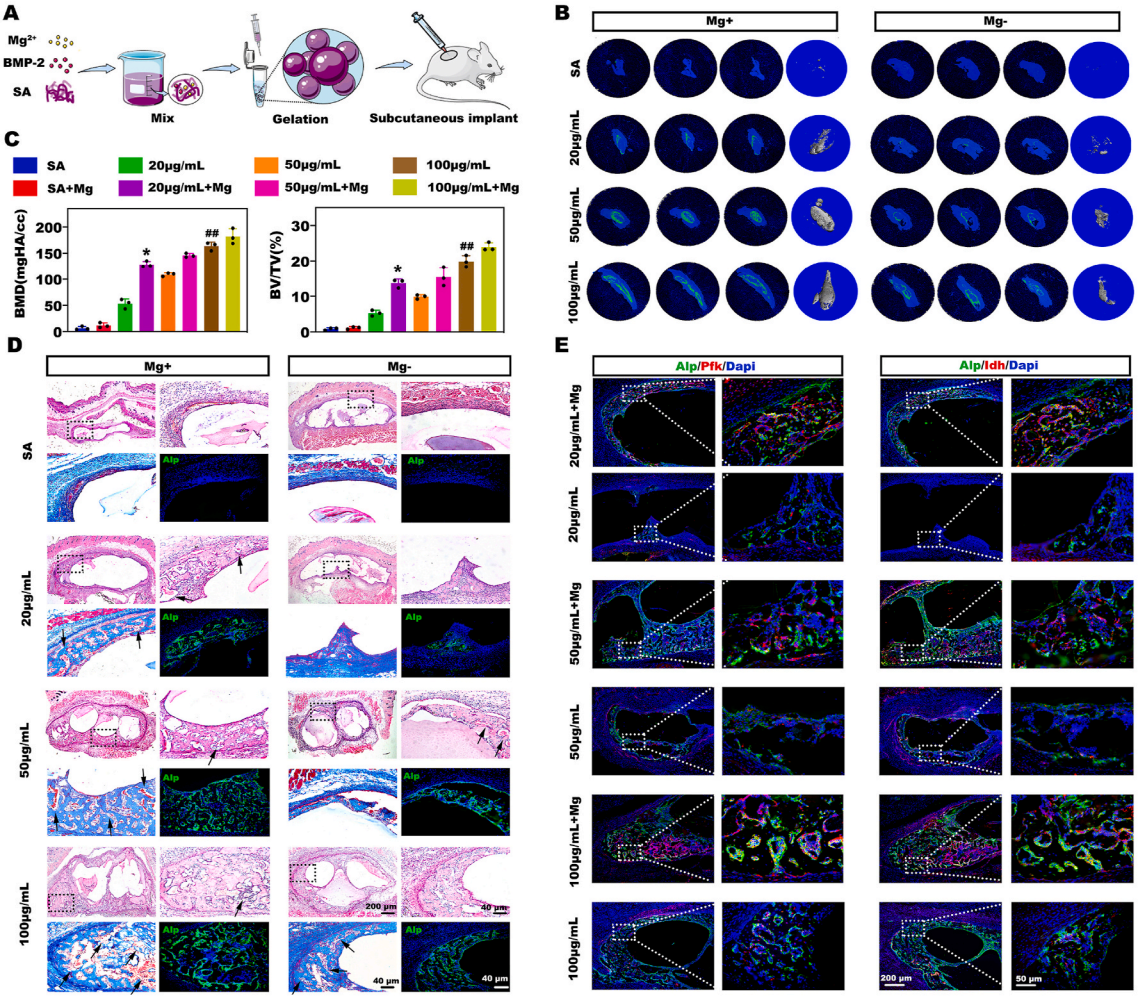

Fig. 2. The Mg-enriched environment resulted in robust ectopic bone formation in the low-dose BMP-2 groups in vivo and elevated expression levels of metabolic enzymes in the bone forming area. A) Schematic of the fabrication and subcutaneous injection of BMP-2/Mg^{2+} microbeads. B) The newly formed bone tissues were evaluated by micro-CT. C) The results of quantitative micro-CT analysis. (* represents $p < 0.05$ in comparison with the 50 μg mL^{-1} group, while ## represents $p < 0.01$ compared to 20 μg mL^{-1} + Mg group). D) Hematoxylin and eosin (H&E), Masson trichrome, and immunofluorescence staining of the bone sections. The arrows in the images indicate the blood vessels. E) Colocalization analysis of Alp and key metabolic enzymes, Pfk and Idh, by immunofluorescence staining.

disturbances, such as diabetes mellitus, impaired BMP-2-induced bone formation [17]. Taken together, we deduced that an inactive metabolic state was responsible for the reduced bone formation after treatment with low-dose BMP-2. More importantly, Mg^{2+} significantly elevated the bioenergetic level, as evidenced by the higher expression levels of metabolic enzymes in the Alp-positive area in the Mg-enriched groups than in the other groups. Mg^{2+} plays a vital role in energy metabolism as a cofactor of ATP and consequently influences the functional states of cells. For instance, a previous study revealed that dietary Mg supplementation improved mitochondrial dysfunction to protect cardiac cells in a diabetes model [22].Based on these findings, we believe that the promotional effects of Mg^{2+} on BMP-2-driven bone formation are closely related to its stimulation of metabolic influx. However, the relationship among energy metabolism, Mg^{2+} and BMP-2-based osteogenesis has not been fully elucidated and needs to be further investigated.

3.3. The rapid metabolic reprogramming triggered by BMP-2 was indispensable for subsequent osteogenesis

To elucidate the relationship among BMP-2-driven osteogenesis, energy metabolism, and Mg^{2+}, we first investigated the relation between BMP-2 and cellular metabolism. Here, to dynamically monitor metabolic adaptation during BMP-2 induction, we sequentially detected OCRs and ECARs of BMSCs. At the early stage of induction, mitochondrial oxygen consumption was increased only slightly, while the glucose-induced glycolysis and glycolysis capacity rapidly surged to levels that were 2.2-fold and 1.8-fold higher than those in the quiescent state, respectively. From day 3 onward, the BMSCs began to exhibit an intensive oxygen demand, and drastic increases in both mitochondrial oxygen consumption and glycolysis were observed on day 7 (Fig. 3A and B). These findings proved that BMP-2 could trigger rapid metabolic reprogramming, characterized by the successive activation of glycolysis and OxPhos. In agreement, the expression levels of osteogenesis- and metabolism-related genes, including the rate-limiting enzymes of glycolysis and the TCA cycle, and the mitochondrial electron transport chain complex were concomitantly increased during BMP-2 induction (Fig. 3C). In particular, glycolytic enzymes were upregulated before OxPhos- and osteogenesis-related genes. Glycolysis and OxPhos are the two basic pathways for energy production, and glycolysis gives rise to less but faster ATP production than OxPhos [35]. We speculated that the rapid activation of glycolysis was a quick response to the acute energy demand for subsequent osteogenesis, while the later strong surge in OxPhos was responsible for the higher bioenergetic level as the degree of osteogenic differentiation intensified. Additionally, the impairment in BMP-2-induced osteogenic differentiation after the pharmacological

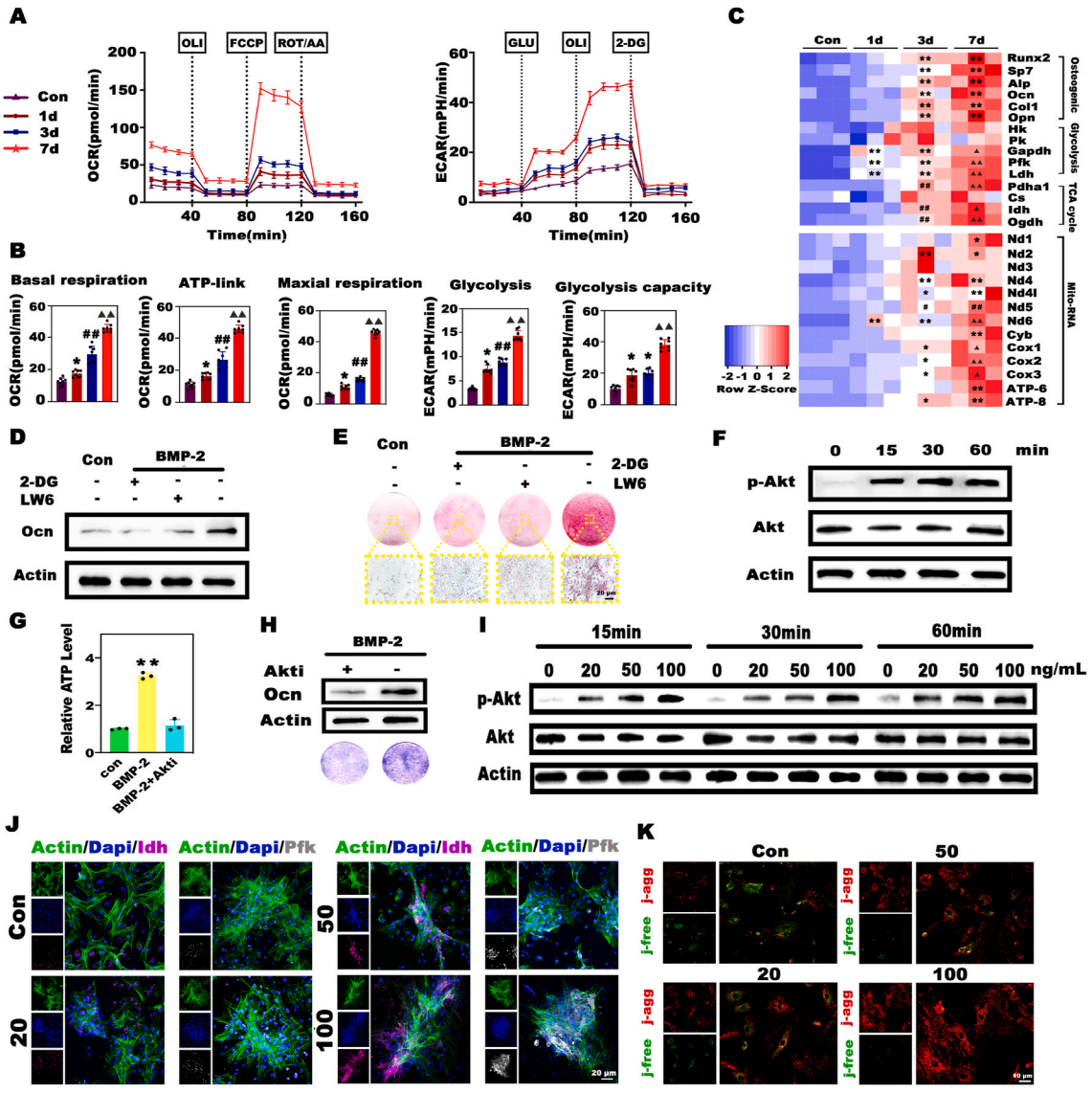

Fig. 3. BMP-2 dose-dependently triggered rapid metabolic reprogramming, which played a decisive role in subsequent osteogenic differentiation. A) Seahorse assay of the OCRs and ECARs of BMSCs during BMP-2 induction. B) Charts depicting the primary parameters calculated from the above Seahorse assay curves. C) Heatmap showing the gene expression profile during BMP-2-mediated osteogenic differentiation. (* and ▲ represent $p < 0.05$ in comparison with the control and 3d groups, respectively; **, ## and ▲▲ represent $p < 0.01$ in comparison with the control, 1d and 3d groups, respectively). D, E) Inhibition of glycolysis and the TCA cycle by 2-DG and LW6 substantially impeded the expression of the Ocn protein and biomineralization. F) BMP-2 stimulated significant phosphorylation of the Akt protein. G, H) ATP synthesis was disrupted and Alp activity was reduced after the treatment of BMSCs with BMP-2 and the Akt inhibitor MK2206 (Akti) (** represents $p < 0.01$ in comparison with the BMP + Akti group). I) BMP-2 activated the Akt pathway in a dose-dependent manner. J) Evaluation of metabolic enzymes in BMSCs treated with different doses of BMP-2 by immunofluorescence staining. K) JC-1 analysis of the mitochondrial membrane potential (ΔΨm) as an indicator of the cellular metabolic state. J-agg indicates cells with aggregated JC-1 (red fluorescence) and high ΔΨm, while j-free indicates cells with free JC-1 (green fluorescence) and low ΔΨm.

inhibition of glycolysis and the TCA cycle by 2-deoxyglucose (2-DG) and LW6 further emphasized the importance of energy metabolism in the osteogenic process (Fig. 3D and E; Fig. S4). Next, we attempted to identify the downstream signaling pathway of BMP-2-triggered metabolic reprogramming. The Akt pathway attracted our attention because it is not only involved in osteogenesis but also an important regulator of metabolic processes [36,37].Western blot analysis revealed that the enhanced phosphorylation of Akt occurred less than 15 min after BMSCs were treated with BMP-2 (Fig. 3F). Blocking the phosphorylation of Akt with MK2206 (Fig. S5A) markedly reduced cellular ATP production (Fig. 3G) and consequently hampered the osteogenesis of BMSCs (Fig. 3H, Fig. S5B). Importantly, BMP-2 triggered metabolic alterations in an obvious dose-dependent manner. Only slight Akt activation was induced by 20 ng mL^{-1} BMP-2, and the elevation in phosphorylation was limited despite the increase in the induction time (Fig. 3I). Similarly, the Pfk and Idh protein expression levels decreased as the BMP-2 dose decreased (Fig. 3J). ΔΨm is the main chemical driving force for ATP synthesis and reflects the cellular metabolic status. To evaluate the metabolic status of BMSCs under different BMP-2 treatments, 5,5′,6,6′-tetrachloro-1,1′,3,3′-tetraethylbenz-imidazolylcarbocyanine iodide (JC-1) was used to determine the ΔΨm. The dye aggregates in mitochondria with high ΔΨm emit red fluorescence, and those in the free form emit green fluorescence. As shown in Fig. 3K, as the BMP-2 dose increased, the green fluorescence gradually decreased, and a considerable increase in red fluorescence was observed, especially in the 100 ng mL^{-1} group, which exhibited the highest red fluorescence intensity. Moreover, the increase in ΔΨm drastically enhanced ATP production as the BMP-2 concentration increased, whereas only a slight increase in the

ATP level was observed in the 20 ng mL^{-1} group (Fig. S6). Taken together, these findings proved that BMP-2 could dose-dependently trigger rapid metabolic reprogramming, characterized by the successive activation of glycolysis and OxPhos, which was indispensable for subsequent osteogenic differentiation. Moreover, the compromised efficacy of low-dose BMP-2 was strongly related to inadequate activation of the metabolic state.

3.4. Mg^{2+} promoted the efficacy of low-dose BMP-2 by elevating the bioenergetic level

As proven above, energy metabolism plays an indispensable role in BMP-2-induced osteogenesis. Next, we assessed whether the promotional effects of Mg^{2+} were related to its regulatory effects on cellular metabolism. First, we evaluated intracellular Mg^{2+} dynamics during BMP-2 induction. Briefly, BMSCs were incubated with mitochondrial markers (red fluorescence) and Mg^{2+} probes (green fluorescence) before

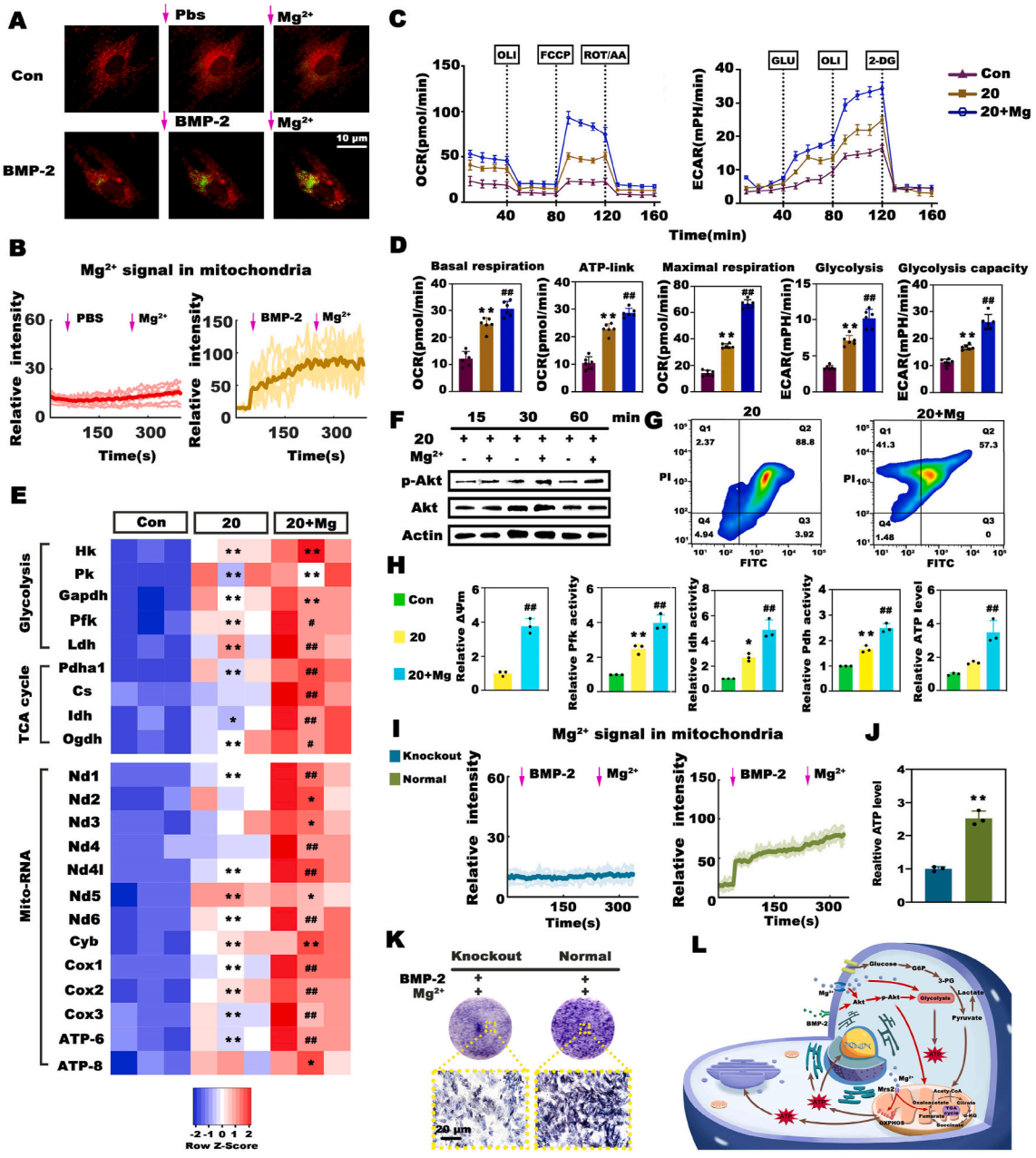

Fig. 4. The promotional effects of Mg^{2+} on BMP-2 resulted from its stimulatory effects on cellular metabolism via the Akt-glycolysis-Mrs2-mitochondrial axis. A) Representative images of intracellular Mg^{2+} dynamics as detected by the Mag-green probe (red fluorescence represents mitochondria). B) Dynamic detection of Mg-green intensity in the mitochondrial region. C) Seahorse analysis of the OCRs and ECARs alterations in BMSCs induced by 20 ng mL^{-1} BMP-2 with or without Mg^{2+} for 7 days. BMSCs cultured in normal medium served as the control. D) Key parameters calculated from the above Seahorse assay curves. E) Heatmap depicting the expression profile of metabolic genes. F) Mg^{2+} addition stimulated the phosphorylation of Akt. G) Analysis of ΔΨm by flow cytometry. Cells in the upper left region exhibited a high ΔΨm, while cells in the lower right region had a low ΔΨm. H) Charts depicting the relative ΔΨm as determined by measuring the mean fluorescence intensity, the activities of metabolic enzymes, and ATP synthesis in the different groups (* and # represent $p < 0.05$, while ** and ## represent $p < 0.01$ in comparison with the control and 20 ng mL^{-1} groups, respectively). I) Changes in the Mg-green intensity in the mitochondria of normal and Mrs2 knockout BMSCs. J) Mrs2 knockout markedly suppressed ATP production in BMSCs treated with BMP-2 and Mg^{2+}. (** represents $p < 0.01$). K) Alp staining of normal and mutant BMSCs. L) Mechanism of the stimulatory effects of Mg^{2+} on the efficacy of BMP-2.

exposure to BMP-2. Intriguingly, BMP-2 triggered a vigorous and rapid increase in the cytosolic Mg-green signal and the aggregation of green fluorescence in the red area, indicating Mg^{2+} influx and mitochondrial Mg^{2+} intake. The addition of Mg^{2+} further strengthened this tendency in the BMP-2 group (Fig. 4A and B). These results suggested a close relation between Mg^{2+} and BMP-2-induced bioactivities. Second, we examined metabolic alterations after culturing BMSCs with relatively low-dose BMP-2 and Mg^{2+} for 7 days. As expected, the addition of Mg^{2+} stimulated the most vigorous mitochondrial oxygen consumption and glycolysis in BMSCs among all the groups (Fig. 4C and D). Then, we explored the mechanism underlying the promotional effects of Mg^{2+} on cellular metabolism. Almost all of the expression levels of metabolic genes involved in glycolysis and OxPhos were remarkably upregulated to a greater extent in the Mg-enriched group than in the group treated with BMP-2 alone (Fig. 4E). The protein levels of the metabolic enzymes were consistently upregulated (Fig. S7). Considering reports that implants containing Mg enhanced osteointegration via the Akt pathway [38], we examined the impacts of Mg^{2+} addition on the activation of Akt signaling. Western blot analysis showed that the Mg-enriched environment favored the phosphorylation of Akt, and the phosphorylation level increased as the incubation time increased (Fig. 4F). In addition, we quantitatively analyzed ΔΨm in combination with JC-1 staining and flow cytometry. As shown in Fig. 4G, significantly more cells with high ΔΨm (41.3%) were observed in the 20 ng mL^{-1}+ Mg group than in the 20 ng mL^{-1} group (2.37%), and the relative ΔΨm was dramatically increased (Fig. 4H). Qualitative analysis of ΔΨm yielded consistent results (Fig. S8). Moreover, the addition of Mg^{2+} substantially increased the activities of Pfk, Pdh (the major link between glycolysis and the TCA cycle), and Idh by at least 1.5-fold compared that in the BMP-2 alone group (Fig. 4H). Consequently, the upregulated expression levels and activities of metabolic enzymes resulted in more ATP synthesis in the Mg-enriched group (Fig. 4H). As mentioned above, BMP-2 initiated obvious mitochondrial Mg^{2+} uptake, and a recent study revealed that the mitochondrial Mg^{2+} influx stimulated by metabolites required the Mg channel Mrs2 [39]. Therefore, we next investigated whether BMP-2-driven mitochondrial Mg^{2+} influx required Mrs2. We designed

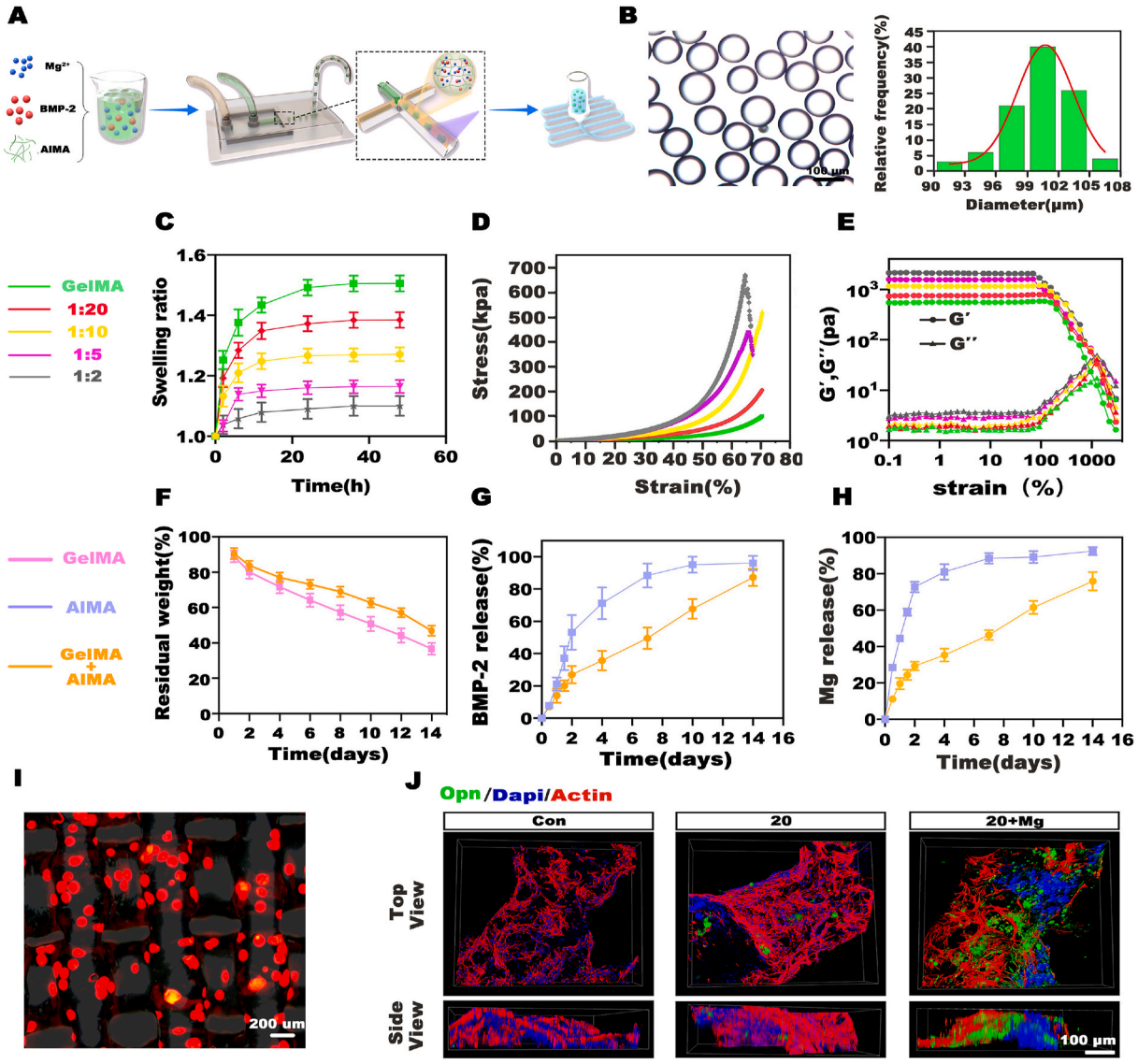

Fig. 5. Fabrication and characterization of the microgel composite hydrogel. A) Procedure used for the fabrication of the microgel composite hydrogel. B) Monodispersed AlMA microgels and particle size distribution. C) Swelling behaviors of hydrogels with different microgel contents. D) Compression tests of hydrogels with different microgel contents. E) Results of the strain-sweep tests. F) Degradation of GelMA hydrogels and composite hydrogels with a 1:10 AlMA/GelMA mass ratio. G, H) Release profile of BMP-2 and Mg^{2+} in AlMA microgels or composite hydrogels. I) The distribution of red fluorescence-labeled AlMA microgels in the hydrogels. J) Expression of Opn in BMSCs on hydrogels as detected by CLSM.

and produced Mrs2 knockout BMSCs via the CRISPR/Cas9 technique (Fig. S9). The depletion of Mrs2 markedly reduced the mitochondrial Mg^{2+} influx (Fig. 4I, Fig. S10A), resulting in a sharp decrease in ATP production and Alp activity in BMSCs treated with BMP-2 and Mg^{2+} (Fig. 4J, K, Fig. S10B). These results highlighted the importance of Mrs2-mediated mitochondrial Mg^{2+} intake in BMP-2-induced metabolic reprogramming and osteogenesis. Collectively, these data suggested that Mg^{2+} improved the efficacy of low-dose BMP-2 by elevating the bioenergetic level to orchestrate energy metabolism and osteogenesis via the Akt-glycolysis-Mrs2-mitochondrial axis (Fig. 4L).

3.5. Fabrication and characterization of the Mg^{2+}-based bioenergetic-driven microgel composite hydrogel as the BMP-2 delivery platform

Optimal platforms are of great importance to transfer the Mg-based bioenergetic-driven BMP-2 delivery system into applications for highly efficient bone regeneration. Although hydrogel microgels are desirable carriers due to their aforementioned unique properties, drawbacks still exist. The mobility of microgels makes them difficult to keep stable at the target area, resulting in off-target side effects. Typically, as shown in Fig. 2B, strip-like bone formation, especially in the high-dose BMP-2 groups, indicated the spread of the microgels along the needle path during injection. To overcome this problem, we embedded the microgels in a matrix material to form a composite structure, in which the matrix material acted as the cement to hold the microgels on the defects, and the microgel fed back to reinforce the mechanical properties of the whole scaffold. Briefly, the microgels were fabricated by photo-crosslinking 6% (w/v) AlMA droplets encapsulating Mg^{2+} and BMP-2 produced from a microfluidic chip. The microgels were collected and then embedded in 6% (w/v) GelMA for subsequent 3D printing (Fig. 5A). Size optimization is substantially important for microgel carriers, as a larger diameter increases the loading capacity of the microgels and facilitates the sustained release of drugs but impairs the injectability at the same time. To fine-tune the microgel size, we adjusted the flow rate ratio of the aqueous and oil phases (Q_{aq}/Q_o) to range from 0.02 to 0.2, resulting in microgels with diameters ranging from 75 μm to 200 μm (Fig. S11). To balance the requirement of drug loading and printability, a moderate size of approximately 100 μm was chosen for the composite preparation. As shown in Fig. 5B, monodisperse AlMA microgels with a diameter of 100.64 ± 3.15 μm were obtained at a Q_{aq}/Q_o of 0.05.

Typically, hydrogels exhibit a swelling-weakening phenomenon when exposed to an aqueous environment in vivo and suffer from a sharp decrease in mechanical strength and the fast release of cargo after swelling, which greatly hinders their application [40]. To investigate the effects of the addition of AlMA microgels to GelMA on the physiological (e.g., swelling and degradability) and mechanical properties of the whole system, we prepared AlMA/GelMA hydrogels with a series of AlMA/GelMA mass ratios ranging from 1:20 to 1:2, and the GelMA hydrogels served as the control. As shown in Fig. 5C, the addition of AlMA microgels decreased the swelling ratio and time to reach swelling equilibrium, indicating that the swelling stability of the whole hydrogel was improved. Accordingly, the compressive strength of the hydrogel in its swelling equilibrium state was also dramatically enhanced as the AlMA microgel content increased to 1:10. As the microgel content was further increased, the compressive strength continued to increase, but the compressive failure strain decreased to approximately 60% (Fig. 5D). Obviously, the addition of AlMA microgels increased the brittleness of the whole system upon evaluation of its strength. The excessive addition of microgels interfered with the gelation of GelMA, which might have been a response to the increase in brittleness. Strain-sweep tests were further performed to examine the rheological characteristics of the different hydrogels. Consistently, as the microgel content increased, the storage modulus (G′) was significantly increased. Comparatively, the collapse of the hydrogel network, namely, the point at which the G′ value began to markedly decrease, was advanced (Fig. 5E). Taking the swelling behavior and the mechanical properties into consideration, we selected 1:10 as the optimal mass ratio of AlMA/GelMA. Moreover, the addition of microgels prolonged the degradation of the scaffolds, partially due to the enhanced swelling stability, which could prevent the burst release of cargoes from the rapidly degrading hydrogel (Fig. 5F).

The short diffusion distance and porous structure of microgels usually lead to the fast release of encapsulated cargoes. In the microgel composite hydrogel, GelMA acted as the secondary barrier around the microgel vesicle to reduce the burst release of cargoes and thus improved the therapeutic effects of the cargoes. To confirm this phenomenon, the release profiles of BMP-2 and Mg^{2+} were measured. 10 μg of BMP-2 and 60 μg of Mg^{2+} were used in each group. The BMP-2 and Mg^{2+} loading efficiencies of AlMA microgels were 95.58 ± 0.59% and 96.27 ± 0.99%, respectively (Fig. S12). In the AlMA microgel group, nearly 21% of BMP-2 (2.02 μg) and 44% of Mg^{2+} (25.68 μg) were released on day 1 (probably attributed to the dilution of the AlMA network after swelling), and approximately 90% of BMP-2 (8.45 μg) and Mg^{2+} (51.09 μg) were released within 8 days. In contrast, after the minimal initial burst release on day 1(1.34 μg of BMP-2, 11.31 μg of Mg^{2+}), the release of BMP-2 and Mg^{2+} in the composite hydrogel became more gradual, and the sustained release lasted for more than 14 days (8.33 μg of BMP-2, 43.83 of μg Mg^{2+} in 14 days) (Fig. 5G and H).

Fluorescence microscopy images revealed that AlMA microgels labeled with red fluorescence were evenly dispersed in the scaffolds (Fig. 5I). Furthermore, the biocompatibility of the hydrogel was evaluated. BMP-2 with or without Mg^{2+} was encapsulated in AlMA microgels, and the composite hydrogels were fabricated as described above. Composite hydrogels without BMP-2 and Mg^{2+} were used as controls. BMSCs were then seeded on the hydrogels and cultured for 14 days, and Opn was selected as the osteogenic differentiation marker. Fig. 5J shows confocal laser scanning microscopy (CLSM) images of the BMSCs on the hydrogels. The BMSCs clearly exhibited a stretched morphology, and the largest Opn-positive area was formed in the BMP-2/Mg^{2+} codelivery group, suggesting the ideal biocompatibility and osteogenic bioactivity of the composite hydrogel.

3.6. In vivo regenerative efficacy evaluation of the bioenergetic-driven low-dose BMP-2 delivery platform

Critical cranial defects in rats were examined to explore the therapeutic effects of the Mg^{2+}-based bioenergetic-driven low-dose BMP-2 delivery platform. After implantation for 4 weeks, samples were collected for radiological and histological analyses. Almost no new bone tissues formed in the blank group, and small amounts of new bone tissues were observed in hydrogels without BMP-2 and Mg (namely, the control group). As expected, the largest amounts of new bones were found in defects treated with the hydrogels containing 100 μg mL^{-1} BMP-2. In contrast, only limited bone regeneration was induced in the 20 μg mL^{-1} BMP-2 group. Notably, the hydrogels with 20 μg mL^{-1} BMP-2 and Mg exerted satisfactory regenerative effects, evidenced by a large number of new bones filling the defects and the nearly completely recovered physiological structure of the skull, as shown in the cross-sectional images (Fig. 6A). Consistently, the bone value and bone mineral density in the 20 μg mL^{-1} + Mg group were markedly higher than those in the 50 μg mL^{-1} group and close to those in the 100 μg mL^{-1} group (Fig. 6B). Similar results were obtained by histological analysis (Fig. 6C). Numerous fibrous tissues without new bones were filled in defects in the blank and control groups, while the increase in the BMP-2 dose promoted bone formation. Interestingly, although the 100 μg mL^{-1} group exhibited the most significant bone regeneration among all groups, the massive application of BMP-2 led to excessive bone formation, as evidenced by the bone formation area exceeding the margin of the cranial bone. In contrast, the 20 μg mL^{-1} + Mg group displayed moderate bone regeneration, which successfully repaired the physiological morphology of the skull, indicating its strong capacity for rapid

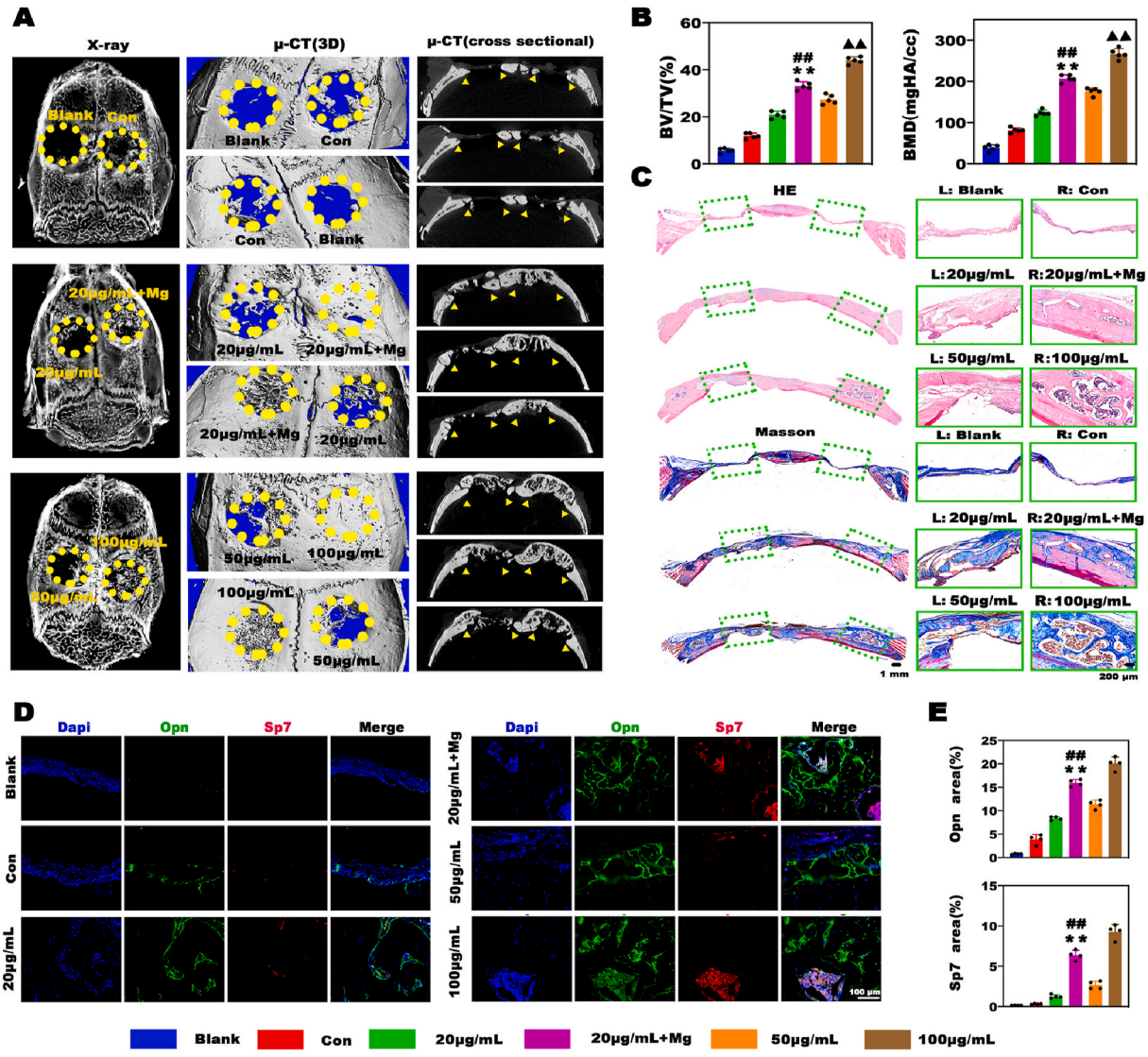

Fig. 6. Evaluation of the efficacy of a Mg^{2+}-based bioenergetic-driven low-dose BMP-2 delivery platform in a rat critical cranial defect model. A) Radiological images of the samples harvested at 4 weeks after implantation. B) Results of the quantitative analysis of bone regeneration. C) H&E and Masson trichrome staining of the decalcified sections. D) Double immunofluorescence staining analysis of the expression of Sp7 and Opn in the different groups. E) The Opn- and Sp7-positive areas were assessed by double immunofluorescence staining, and 4 random images from each group were selected for evaluation. (**, ## and ▲▲ represent $p < 0.01$ in comparison with the 20, 50 μg mL^{-1} and 20 μg mL^{-1} + Mg groups, respectively).

and precise bone regeneration. We further examined the expression levels of the osteogenesis hallmarks Sp7 and Opn by double immunofluorescence staining, and the results are displayed in Fig. 6D and E. There were almost no Opn- and Sp7-positive areas in the blank group and relatively few positive areas in the control and 20 μg mL^{-1} groups, indicating inactive bone repair. Comparatively, the Opn-positive and Sp7-positive areas in the 20 μg mL^{-1} + Mg group were substantially larger than those in the 20 and 50 μg mL^{-1} groups, indicating a robust bone remodeling process. In conclusion, the bioenergetic-driven low-dose BMP-2 delivery platform with Mg as an energy propellant exhibited great potential for rapid and precise bone regeneration.

4. Conclusion

In conclusion, our study demonstrated that orchestration of energy metabolism and osteogenesis by Mg^{2+} successfully amplify the efficacy of low-dose BMP-2, leading to efficacious bone regeneration. We revealed the previously unclear relation between the ineffectiveness of BMP-2 and inadequate energy status, and highlighted that Mg^{2+} markedly promoted the osteoinductivity of BMP-2 via activating energy-producing metabolic pathways. Furthermore, microgel composite hydrogels were fabricated as the BMP-2/Mg^{2+} codelivery platform. The composite structure endowed the hydrogels with a prolonged cargo release and improved mechanical properties. More importantly, the low-dose BMP-2/Mg^{2+} codelivery platform induced high-performance bone regeneration in rat critical bone defects, providing a promising strategy for the clinical treatment of bone defects.

CRediT authorship contribution statement

Sihan Lin: Conceptualization, Methodology, Investigation, Data curation, Formal analysis, Writing – original draft. **Shi Yin:** Methodology, Investigation, Data curation. **Junfeng Shi:** Methodology, Investigation. **Guangzheng Yang:** Methodology, Funding acquisition. **Xutao Wen:** Investigation. **Wenjie Zhang:** Conceptualization. **Mingliang Zhou:** Conceptualization, Methodology, Funding acquisition, Investigation, Writing – review & editing. **Xinquan Jiang:** Conceptualization, Funding acquisition, Project administration, Supervision, Writing –

review & editing.

Declaration of competing interest

The authors declare no conflict of interest.

Acknowledgements

S.L. and S.Y. contributed equally to this work. This work was financially supported by the National Natural Science Foundation of China (No.82130027, No.81921002 and No.31900971), Innovative Research Team of High-level Local Universities in Shanghai (SHSMU-ZLCX20212400), and Shanghai Sailing Program (21YF1424400).

Appendix A. Supplementary data

Supplementary data to this article can be found online at https://doi.org/10.1016/j.bioactmat.2022.03.024.

References

[1] V.S. Salazar, L.W. Gamer, V. Rosen, BMP signalling in skeletal development, disease and repair, Nat. Rev. Endocrinol. 12 (4) (2016) 203–221.
[2] A.W. James, G. LaChaud, J. Shen, G. Asatrian, V. Nguyen, X. Zhang, K. Ting, C. Soo, A review of the clinical side effects of bone morphogenetic protein-2, Tissue Eng. B Rev. 22 (4) (2016) 284–297.
[3] C.J. Kowalczewski, J.M. Saul, Surface-mediated delivery of siRNA from fibrin hydrogels for knockdown of the BMP-2 binding antagonist noggin, Acta Biomater 25 (2015) 109–120.
[4] R.E. De la Vega, A. Atasoy-Zeybek, J.A. Panos, V.A.N. G M, C.H. Evans, E. R. Balmayor, Gene therapy for bone healing: lessons learned and new approaches, Transl. Res. 236 (2021) 1–16.
[5] P.S. Lienemann, Q. Vallmajo-Martin, P. Papageorgiou, U. Blache, S. Metzger, A. S. Kivelio, V. Milleret, A. Sala, S. Hoehnel, A. Roch, R. Reuten, M. Koch, O. Naveiras, F.E. Weber, W. Weber, M.P. Lutolf, M. Ehrbar, Smart hydrogels for the augmentation of bone regeneration by endogenous mesenchymal progenitor cell recruitment, Adv. Sci. 7 (7) (2020) 1903395.
[6] S. Zwingenberger, R. Langanke, C. Vater, G. Lee, E. Niederlohmann, M. Sensenschmidt, A. Jacobi, R. Bernhardt, M. Muders, S. Rammelt, S. Knaack, M. Gelinsky, K.P. Günther, S.B. Goodman, M. Stiehler, The effect of SDF-1α on low dose BMP-2 mediated bone regeneration by release from heparinized mineralized collagen type I matrix scaffolds in a murine critical size bone defect model, J. Biomed. Mater. Res. 104 (9) (2016) 2126–2134.
[7] E. Dashtimoghadam, F. Fahimipour, N. Tongas, L. Tayebi, Microfluidic fabrication of microcarriers with sequential delivery of VEGF and BMP-2 for bone regeneration, Sci. Rep. 10 (1) (2020) 11764.
[8] A. Ho-Shui-Ling, J. Bolander, L.E. Rustom, A.W. Johnson, F.P. Luyten, C. Picart, Bone regeneration strategies: engineered scaffolds, bioactive molecules and stem cells current stage and future perspectives, Biomaterials 180 (2018) 143–162.
[9] D.B. Raina, I. Qayoom, D. Larsson, M.H. Zheng, A. Kumar, H. Isaksson, L. Lidgren, M. Tagil, Guided tissue engineering for healing of cancellous and cortical bone using a combination of biomaterial based scaffolding and local bone active molecule delivery, Biomaterials 188 (2019) 38–49.
[10] F. Mingozzi, K.A. High, Therapeutic in vivo gene transfer for genetic disease using AAV: progress and challenges, Nat. Rev. Genet. 12 (5) (2011) 341–355.
[11] H. Sun, J. Wang, F. Deng, Y. Liu, X. Zhuang, J. Xu, L. Li, Co-delivery and controlled release of stromal cell-derived factor-1α chemically conjugated on collagen scaffolds enhances bone morphogenetic protein-2-driven osteogenesis in rats, Mol. Med. Rep. 14 (1) (2016) 737–745.
[12] K.J. Motyl, A.R. Guntur, A.L. Carvalho, C.J. Rosen, Energy metabolism of bone, Toxicol. Pathol. 45 (7) (2017) 887–893.
[13] J. Loeffler, G.N. Duda, F.A. Sass, A. Dienelt, The metabolic microenvironment steers bone tissue regeneration, Trends Endocrinol. Metabol. 29 (2) (2018) 99–110.
[14] J. Wei, J. Shimazu, P. Munevver, Makinistoglu, A. Maurizi, D. Kajimura, H. Zong, T. Takarada, T. Iezaki, Jeffrey E. Pessin, E. Hinoi, G. Karsenty, Glucose uptake and Runx2 synergize to orchestrate osteoblast differentiation and bone formation, Cell 161 (7) (2015) 1576–1591.
[15] C. Ma, X. Tian, J.P. Kim, D. Xie, X. Ao, D. Shan, Q. Lin, M.R. Hudock, X. Bai, J. Yang, Citrate-based materials fuel human stem cells by metabonegenic regulation, Proc. Natl. Acad. Sci. U. S. A. 115 (50) (2018) E11741–E11750.
[16] L. Grgurevic, G.L. Christensen, T.J. Schulz, S. Vukicevic, Bone morphogenetic proteins in inflammation, glucose homeostasis and adipose tissue energy metabolism, Cytokine Growth Factor Rev 27 (2016) 105–118.
[17] R.B. de Santana, P.C. Trackman, Effect of targeted delivery of bone morphogenetic protein-2 on bone formation in type 1 diabetes, Int. J. Oral Maxillofac. Implants 30 (3) (2015) 707–714.
[18] H. Li, D. Liu, C.Q. Zhao, L.S. Jiang, L.Y. Dai, Insulin potentiates the proliferation and bone morphogenetic protein-2-induced osteogenic differentiation of rat spinal ligament cells via extracellular signal-regulated kinase and phosphatidylinositol 3-kinase, Spine 33 (22) (2008) 2394–2402.
[19] J. Zhang, L. Tang, H. Qi, Q. Zhao, Y. Liu, Y. Zhang, Dual function of magnesium in bone biomineralization, Adv Healthc Mater 8 (21) (2019), e1901030.
[20] L. Garfinkel, D. Garfinkel, Magnesium regulation of the glycolytic pathway and the enzymes involved, Magnesium 4 (2–3) (1985) 60–72.
[21] I. Pilchova, K. Klacanova, Z. Tatarkova, P. Kaplan, P. Racay, The involvement of Mg(2+) in regulation of cellular and mitochondrial functions, Oxid. Med. Cell. Longev. (2017) 6797460, 2017.
[22] M. Liu, E.M. Jeong, H. Liu, A. Xie, E.Y. So, G. Shi, G.E. Jeong, A. Zhou, S. C. Dudley Jr., Magnesium supplementation improves diabetic mitochondrial and cardiac diastolic function, JCI Insight 4 (1) (2019), e123182.
[23] A.C. Daly, L. Riley, T. Segura, J.A. Burdick, Hydrogel microparticles for biomedical applications, Nat. Rev. Mater. 5 (1) (2020) 20–43.
[24] F. Topuz, A. Henke, W. Richtering, J. Groll, Magnesium ions and alginate do form hydrogels: a rheological study, Soft Matter 8 (18) (2012) 4877–4881.
[25] W. Zhang, C. Zhu, D. Ye, L. Xu, X. Zhang, Q. Wu, X. Zhang, D.L. Kaplan, X. Jiang, Porous silk scaffolds for delivery of growth factors and stem cells to enhance bone regeneration, PLoS One 9 (7) (2014), e102371.
[26] M. Calderon-Dominguez, M. Alcala, D. Sebastian, A. Zorzano, M. Viana, D. Serra, L. Herrero, Brown adipose tissue bioenergetics: a new methodological approach, Adv. Sci. 4 (4) (2017) 1600274.
[27] H.M. Chow, J.K. Sun, R.P. Hart, K.K. Cheng, C.H.L. Hung, T.M. Lau, K.M. Kwan, Low-density lipoprotein receptor-related protein 6 cell surface availability regulates fuel metabolism in astrocytes, Adv. Sci. 8 (16) (2021), e2004993.
[28] F. Gao, Z. Xu, Q. Liang, H. Li, L. Peng, M. Wu, X. Zhao, X. Cui, C. Ruan, W. Liu, Osteochondral regeneration with 3D-printed biodegradable high-strength supramolecular polymer reinforced-gelatin hydrogel scaffolds, Adv. Sci. 6 (15) (2019) 1900867.
[29] X. Sun, Q. Lang, H. Zhang, L. Cheng, Y. Zhang, G. Pan, X. Zhao, H. Yang, Y. Zhang, H.A. Santos, W. Cui, Electrospun photocrosslinkable hydrogel fibrous scaffolds for rapid in vivo vascularized skin flap regeneration, Adv. Funct. Mater. 27 (2) (2017) 1604617.
[30] X. Zhao, S. Liu, L. Yildirimer, H. Zhao, R. Ding, H. Wang, W. Cui, D. Weitz, Injectable stem cell-laden photocrosslinkable microspheres fabricated using microfluidics for rapid generation of osteogenic tissue constructs, Adv. Funct. Mater. 26 (17) (2016) 2809–2819.
[31] W. Chu, T. Li, G. Jia, Y. Chang, Z. Liu, J. Pei, D. Yu, Z. Zhai, Exposure to high levels of magnesium disrupts bone mineralization in vitro and in vivo, Ann. Transl. Med. 8 (21) (2020) 1419.
[32] W.C. Lu, E. Pringa, L. Chou, Effect of magnesium on the osteogenesis of normal human osteoblasts, Magnes. Res. 30 (2) (2017) 42–52.
[33] S. Wee, W.R. Gombotz, Protein release from alginate matrices, Adv. Drug Deliv. Rev. 31 (3) (1998) 267–285.
[34] N. Satoh, Y. Yamada, Y. Kinugasa, N. Takakura, Angiopoietin-1 alters tumor growth by stabilizing blood vessels or by promoting angiogenesis, Cancer Sci 99 (12) (2008) 2373–2379.
[35] G. Yellen, Fueling thought: management of glycolysis and oxidative phosphorylation in neuronal metabolism, J. Cell Biol. 217 (7) (2018) 2235–2246.
[36] Y.H. Cheng, J.C. Dong, Q. Bian, Small molecules for mesenchymal stem cell fate determination, World J. Stem Cell. 11 (12) (2019) 1084–1103.
[37] G. Hoxhaj, B.D. Manning, The PI3K-AKT network at the interface of oncogenic signalling and cancer metabolism, Nat. Rev. Cancer 20 (2) (2020) 74–88.
[38] Z. Wang, X. Wang, J. Pei, Y. Tian, J. Zhang, C. Jiang, J. Huang, Z. Pang, Y. Cao, X. Wang, S. An, X. Wang, H. Huang, G. Yuan, Z. Yan, Degradation and osteogenic induction of a SrHPO4-coated Mg-Nd-Zn-Zr alloy intramedullary nail in a rat femoral shaft fracture model, Biomaterials 247 (2020) 119962.
[39] C.C. Daw, K. Ramachandran, B.T. Enslow, S. Maity, B. Bursic, M.J. Novello, C. S. Rubannelsonkumar, A.H. Mashal, J. Ravichandran, T.M. Bakewell, W. Wang, K. Li, T.R. Madaris, C.E. Shannon, L. Norton, S. Kandala, J. Caplan, S. Srikantan, P. B. Stathopulos, W.B. Reeves, M. Madesh, Lactate elicits ER-mitochondrial Mg(2+) dynamics to integrate cellular metabolism, Cell 183 (2) (2020) 474–489 e17.
[40] F. Wu, Y. Pang, J. Liu, Swelling-strengthening hydrogels by embedding with deformable nanobarriers, Nat. Commun. 11 (1) (2020) 4502.